Supplemental Experimental Procedures

Materials. Ytterbium (III) acetate hydrate (99.9%), yttrium (III) acetate hydrate (99.9%), erbium (III) acetate hydrate (99.9%), oleic acid (90%), 1-octadecene (90%), sodium hydroxide (NaOH; >98%), ammonium fluoride (NH_4F; >98%), and cyclohexane were purchased from Sigma-Aldrich. All chemicals were used as received without further purification.

Nanocrystal synthesis. $NaYF_4$:Yb^{3+}/Er^{3+}(18/2 mol%) nanocrystals were synthesized according to previous reports. Typically, a 4-mL aqueous solution of $Ln(CH_3CO_2)_3$ (0.2 M, Ln= Y, Yb, and Er) was added to a 50-mL flask containing 6-mL oleic acid and 14-mL 1-octadecene. The reaction mixture was heated to 150 °C for one hour with stirring to remove water from the solution. After cooling down to room temperature, 12-mL of methanol solution containing NH_4F (3.2 mmol) and NaOH (2 mmol) was added under stirring for 30 min. After the methanol evaporated, the solution was heated to 290 °C under argon for 2 h and then cooled to room temperature. The resulting nanoparticles were washed several times with ethanol and redispersed in 4 mL of cyclohexane.

Fabrication of Al rod-SiO_2-Al film antennas. As shown in Figure S2, firstly, a 100-nm thick Al film was first deposited on a cleaned silicon substrate using an electron beam evaporator (Kurt J. Lesker), followed by spin-coating of a layer of poly(methyl methacrylate) (PMMA 950K A4, Microchem) on the surface of the Al film as a positive resist at a rotation speed of 3500 rpm. The resist was solidified by baking at 150 ^{o}C for three minutes. Next, the rod-shaped nanoholes with different lengths and widths were fabricated by electron beam lithography (Raith, eLINE Plus) at 30 kV. Subsequently, 15 nm SiO_2 and 40 nm Al were sequentially deposited on the top layer to form the metal-spacer-metal gaps. Finally, the photoresist was washed off in acetone to obtain plasmonic pixel arrays.

Assembly of upconversion nanoparticles. The obtained spherical upconversion particles (~20 nm in diameter) capped with oleic-acid ligands (length ~1 nm) were diluted and suspended in cyclohexane. One drop of the solution was dropped onto the template, followed by spin coating at 3000 rpm.

Physical measurements. Transmission electron microscopy (TEM) was performed on a JEOL-JEM 2100F electron microscope at an acceleration voltage of 100 kV. Scanning electron microscopy (SEM) was carried out with a JEOL-JSM-6701F electron microscope at 5 kV.

Optical characterizations. Reflectance spectra were recorded using a microspectrophotometer (CRIAC) and collected using a 100× lens (NA = 0.9). The reflectivity of a bulk Al film was measured as a reference. Optical characterization was performed using a Nikon Ti-U microscope coupled with a 980 nm continuous-wave laser. The 980 nm excitation laser was defocused through the objective (100×, 0.9 NA) to a 10-μm diameter spot on the sample. The luminescence signal passed through an 850 nm short-pass fluorescence filter and was collected by a camera (Andor Ixon Ultra) and a spectrometer (Andor Newton). The polarized upconversion spectrum was measured by placing an NIR polarization filter and a half waveplate in front of the laser operating at 980 nm to adjust the polarization direction of the laser source. Another polarizer filter for visible light was placed in front of the detector to record emission polarization (Figure S5).

Theoretical modeling. 3D Finite-difference time-domain simulations were performed using a commercial simulation software package. The refractive indices of the Si (silicon), SiO_2 (glass) and Al (aluminum) elements of the structures were all set to the values in the material data base of lumerical FDTD (Palik)[S1]. The refractive index of the UCNPs was set to 1.47[S2]. To simulate optical field distributions and plasmon resonance modes, periodic boundary conditions were used along the *x*- and *y*-axes, while a perfectly matched layer was used along the *z*-axis. The finest mesh size was set to 1 nm in the structure. Broadband plane waves propagating along the z-axis and polarized along either the x-axis or y-axis were used to obtain reflection spectra (Figure 2A) and the profiles of the localized electric fields (Figure S4). Reflection spectra were obtained by placing a surface power monitor perpendicular to the z-axis behind the excitation source (in air) and integrating the power flux through the surface

for each wavelength of the source. Similarly, electric field profiles were simulated by placing a surface monitor perpendicular to the z-axis and by selecting the resonance at the wavelength of interest.

For polarization-dependent excitation and emission enhancement factors, the simulation was based on a simplified excited state absorption (ESA)-mediated upconversion process (Figure S13)[S3]. In the ESA process, the upconversion signal is related to the fourth power of the localized E-field amplitude enhancement. In the case of weak excitation without reaching saturation, the excitation enhancement of an upconversion emitter near a plasmon antenna can be expressed as:

$$f_{ex}^{\theta} = \frac{|\mu \cdot E_{\theta}|^4}{|\mu \cdot E_0|^4} \frac{\gamma_{T10}^0}{\gamma_{T10}^{\theta}} \quad (1)$$

where μ is the electric transition of the electric dipole moment, and E_θ and E_0 are the polarization-dependent localized *E*-field under the excitation of plasmon resonance and the incident field, respectively. γ_{T10}^{θ} and γ_{T10}^{0} represent the total decay rate from the intermediate state 1⟩ to the ground state 0⟩ ($^4I_{11/2}$ to $^4I_{15/2}$ for Er^{3+}) in the vicinity and absence of the metallic nanostructure. θ represents the polarization angle of the incident light or the dipole orientation.

For an isolated emitter, the intrinsic quantum efficiency for the emission transition from emission level 2⟩ to ground state 0⟩ ($^4S_{3/2}$ to $^4I_{15/2}$ or $^4F_{9/2}$ to $^4I_{15/2}$ for Er^{3+}) can be expressed as:

$$\eta_0 = \frac{\gamma_{20}^{R0}}{\gamma_{20}^{R0} + \gamma_{20}^{NR0}} \quad (2)$$

where γ_{20}^{R0} is the radiative decay rate and $\gamma_{20}^{\mathrm{NR0}}$ is the non-radiative decay rate (related to the intrinsic losses of the emitter). For an emitter located in the vicinity of a metallic nanostructure, the total decay rate changes to:

$$\gamma_{20}^{T} = \gamma_{20}^{R} + \gamma_{20}^{NR} + \gamma_{20}^{NR0} \quad (3)$$

where γ_{20}^{R} is the cavity–accelerated decay rate of the emitter and γ_{20}^{NR} represents the non-radiative decay rate due to energy dissipated into the metallic nanostructure. The antenna efficiency of the nanostructure is defined as:

$$\eta_a = \frac{\gamma_{20}^{R}}{\gamma_{20}^{R} + \gamma_{20}^{NR}} \quad (4)$$

Further considering the dipole orientation (θ), the antenna efficiency is defined as:

$$\eta_a^{\theta} = \frac{\gamma_{20}^{R\theta}}{\gamma_{20}^{R\theta} + \gamma_{20}^{NR\theta}} \quad (5)$$

The Purcell factor *F*, defined as the increase in the radiative decay rate, can be expressed as:

$$F_{\theta} = \frac{\gamma_{20}^{R\theta}}{\gamma_{20}^{R0}}. \quad (6)$$

Since the antenna-modified quantum efficiency $\eta(\omega)$ is related to the intrinsic quantum efficiency $\eta_0(\omega)$, the Purcell factor *F(ω)* and the antenna efficiency $\eta_a(\omega)$ at the emission frequency. Therefore, the emission enhancement f_{em}^{θ} of the emitter can be calculated according to:

$$f_{em}^{\theta} = \frac{\eta_{\theta}(\omega)}{\eta_0(\omega)} = \frac{1}{\frac{1-\eta_0(\omega)}{F_{\theta}(\omega)} + \eta_0(\omega)/\eta_a^{\theta}(\omega)} \quad (7)$$

In our 3D-FDTD farmwork, plane waves were also used to determine the excitation field enhancement $(E_\theta/E_0)^4$ of UCNPs at given locations of the emitters for incident polarization angles. Data for $\gamma_{T10}^{0}/\gamma_{T10}^{\theta}$, $F_{\theta}(\omega)$, and $\eta_a^{\theta}(\omega)$ were calculated by monitoring the property of a single point dipole source. In the FDTD simulation, decay

rates are proportional to the corresponding power ratios, which means that all quantities can be computed as the power emitted by a classical oscillating dipole near the plasmon structure, and this is normalized by the power emitted by a classical oscillating dipole in vacuum. The radiative power and the total power were collected by integrating the Poynting vector over an outer surface enclosing the emitter-cavity system and an inner surface enclosing only the dipole emitter, respectively. This method has been widely applied in the calculation of the transition dynamics of fluorescent molecules near metallic nanostructures or in dielectric environment[S4]. The related simulation package is available on the Ansys Lumerical FDTD website, with the simulation file named "fluorescence_enhancement.fsp". We define that P_{mn}^{R} is the power reaching the far field and P_{mn}^{T} is the total power emitted by the dipole source, including the power dissipated to the metal. Here, the subscripts represent the electric transitions from *m* to *n*, where *m* = 1 or 2 and *n* = 0. The quantities can then be given as $\gamma_{T10}^{0}/\gamma_{T10}^{\theta} = P_{T10}^{T0}/P_{T10}^{T\theta}$, $F_{\theta} = \gamma_{20}^{R\theta}/\gamma_{20}^{R0} = P_{20}^{R\theta}/P_{20}^{R0}$ and $\eta_{a}^{\theta} = \gamma_{20}^{R\theta}/(\gamma_{20}^{R\theta} + \gamma_{20}^{NR\theta}) = P_{20}^{R\theta}/P_{20}^{T\theta}$, where the symbols superscripted with 0 correspond to the quantities for the isolated emitter in uniform background medium. For polarization properties, the power (*P*) was recorded by tuning the orientation of the dipole source from 0° to 360° in X-Y plane. The distance between the emitter and the antennas was set to 5 nm and 10 nm, respectively. The data collected by simulations were further transferred to the formulas for calculating f_{ex}^{θ} and f_{em}^{θ}, which are further plotted as a function of polarization angle (Figure 2I, Figure 3E and Figure S14-S17).

Numerical simulations. A general sensitizer-activator upconversion system involving two- and three-photon population processes was used for numerical simulations. To simplify the system, we considered basic optical transitions in lanthanide doped UCNPs, including sensitizer absorption and intrinsic decay of excited states. However, we disregarded secondary processes, such as activator absorption and cross-relaxation between activators. Thus, the general trend of population evolution can be revealed despite the selection of sensitizers or activators. The simulation for this simplified system was performed based on the following rate equations:

$$n'_{s2}[t] = P_{980}n_{s1}[t] - w_s n_{s2}[t] - (c_1 n_1[t] + c_2 n_2[t])n_{s2}[t] \quad (8)$$

$$n'_{s1}[t] = -n'_{s2}[t] \quad (9)$$

$$n'_{1}[t] = -c_1 n_{s2}[t]n_1[t] + w_2 n_2[t] + b_{31}w_3 n_3[t] \quad (10)$$

$$n'_{2}[t] = c_1 n_{s2}[t]n_1[t] + b_{32}w_3 n_3[t] - w_2 n_2[t] - c_2 n_{s2}[t]n_2[t] \quad (11)$$

$$n'_{3}[t] = c_2 n_{s2}[t]n_2[t] - w_3 n_3[t] \quad (12)$$

Here, P_{980} is the absorption rate of sensitizer; w_s is the intrinsic decay rate of the sensitizer; w_i is the intrinsic excited state decay rate of the activator; b_{ij} is the branching ratio for activator decaying from excited state i to j; c_i is the upconversion coefficient between the sensitizer and activator residing at the excited state i. The estimated values of these parameters were summarized in Table S1. The steady state population density evolution of excited state (n_3) for two photon population process can be obtained by solving the rate equation at different P_{980} values. Moreover, the dependence of the slope value on different P_{980} was calculated by derivation. It should be noted that the modeling here means to build a universal sensitizer-activator upconversion system involving essential transition processes for the general lanthanide-doped upconversion. The simulation results can reveal the general trends of the slope change regardless of the selection of sensitizers or activators.

Supplemental Figures

Table S1. Parameters used in numerical simulations of the sensitizer-activator upconversion system[S5].

Kinetic Parameters		
Intrinsic decay constants (s^{-1})		
w_s	w_2	w_3
1000	500	1000
Upconversion coefficients (cm^3s^{-1})		
c_1	c_2	
1×10^{-17}	1×10^{-17}	
Branching ratios		
b_{31}	b_{32}	
0.3	0.7	

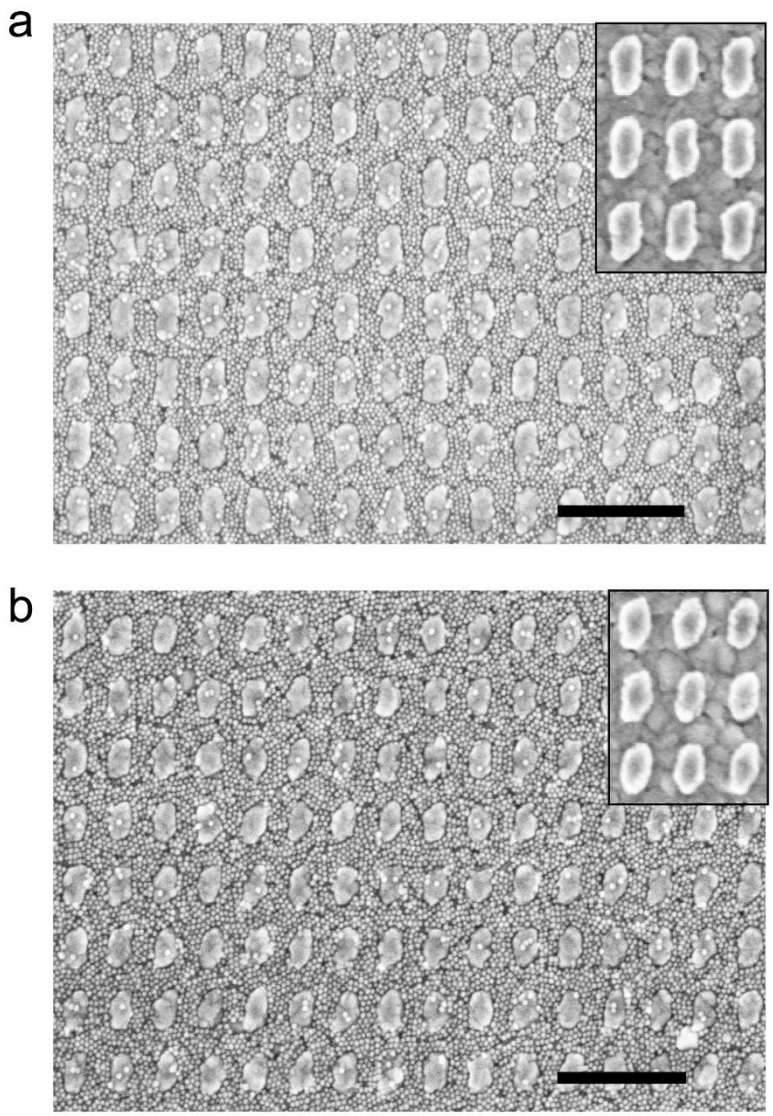

Figure S1. SEM images of the plasmon-emitter hybrid structure with UCNPs located around MIM antennas. Longitudinal length (L_y): 170 nm in (**a**) and 130 nm in (**b**). Scale bar: 500 nm.

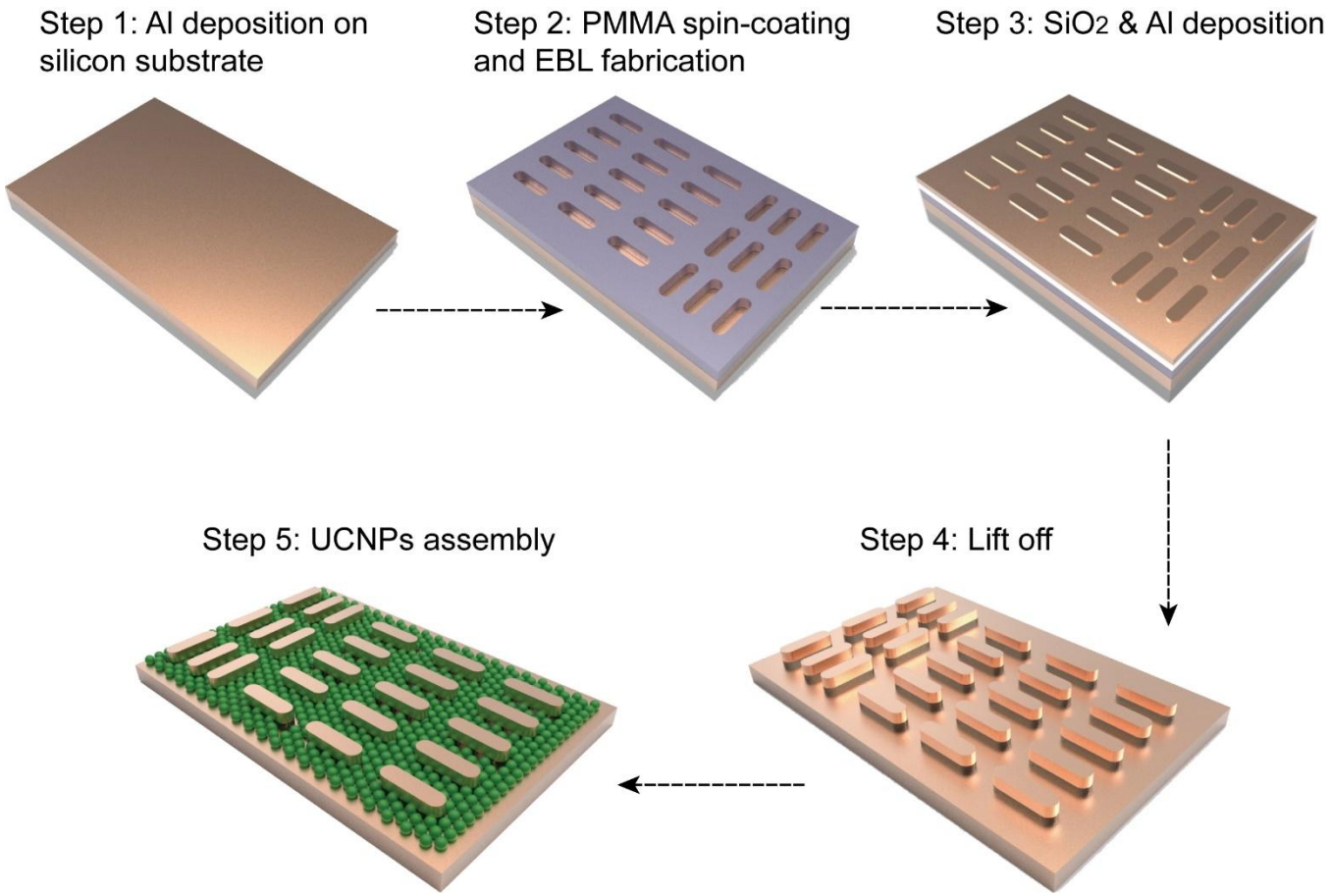

Figure S2. Schematic of the fabrication process of plasmonic antennas coupled with upconversion nanoparticles.

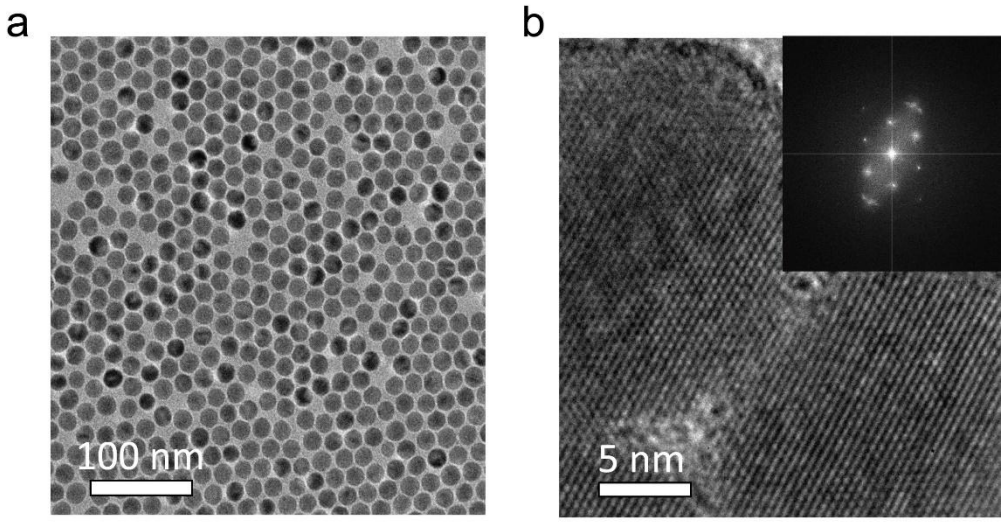

Figure S3. TEM (**a**) and HRTEM (**b**) images of as-prepared $NaYF_4$:Yb/Er (18/2%) nanoparticles with a diameter of about 20 nm.

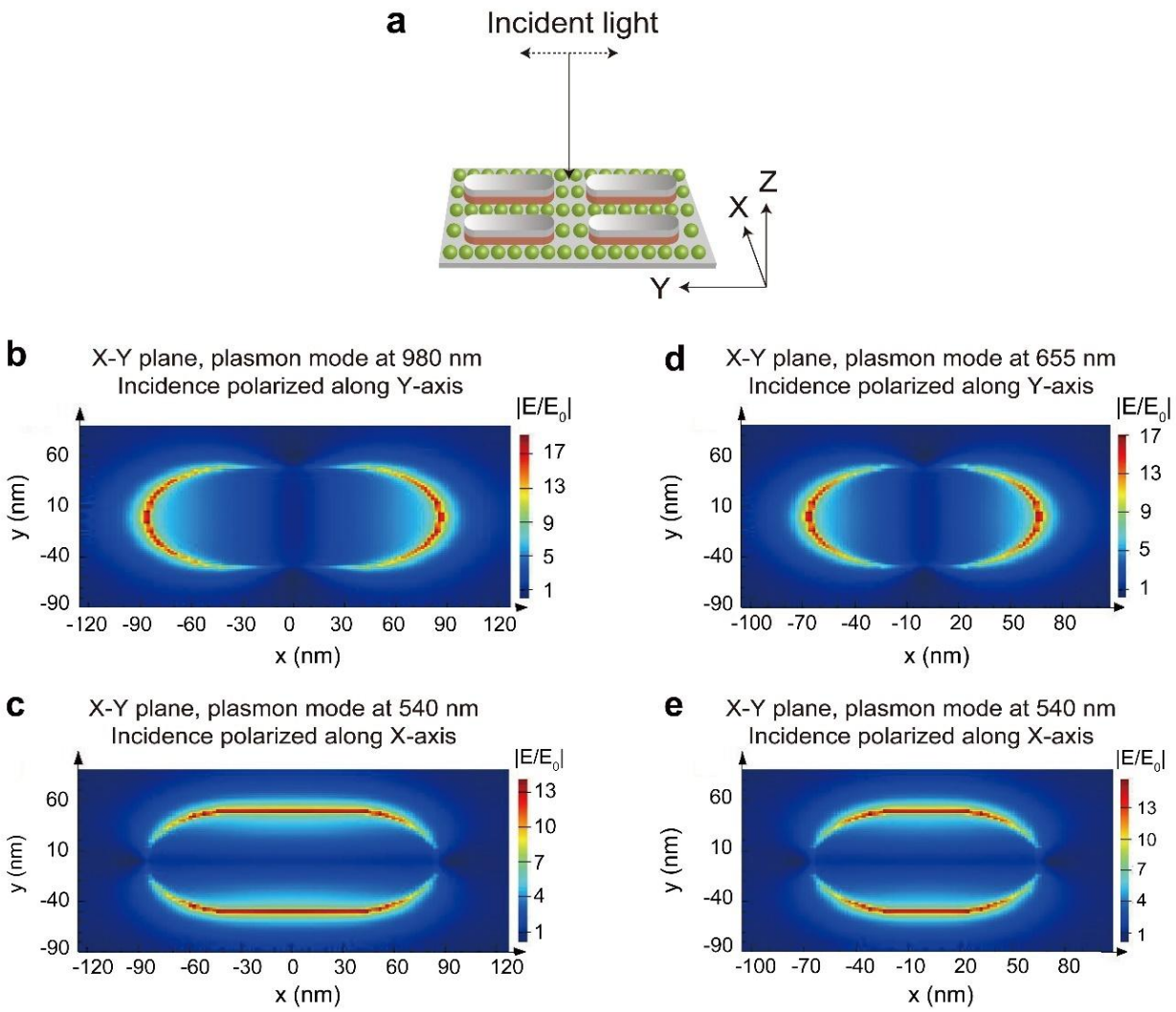

Figure S4. (**a**) Incident light is sent normally to the X-Y plane with the polarization direction parallel to either the *x*-axis or the *y*-axis. Simulated electric near-field distributions around antenna-170 (**b,c**) and antenna-130 (**d,e**) coupled with UCNPs.

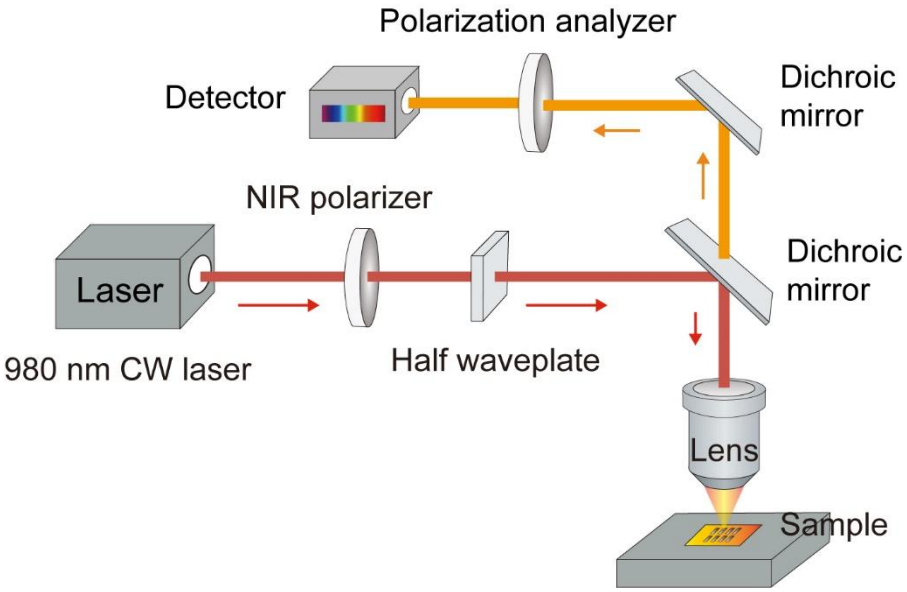

Figure S5. The experimental setup used for upconversion luminescence measurements.

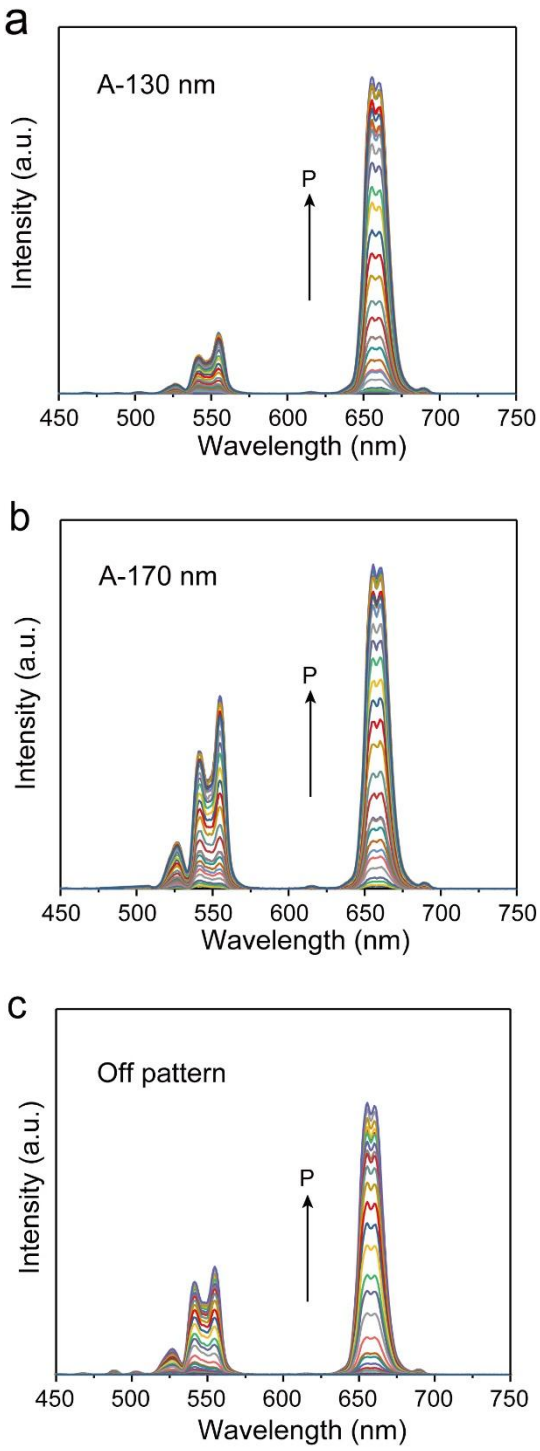

Figure S6. Upconversion photoluminescence spectra recorded under different excitation power densities for three samples: UCNPs deposited on antenna-130 (**a**), antenna-170 (**b**), and Al film without antennas (**c**).

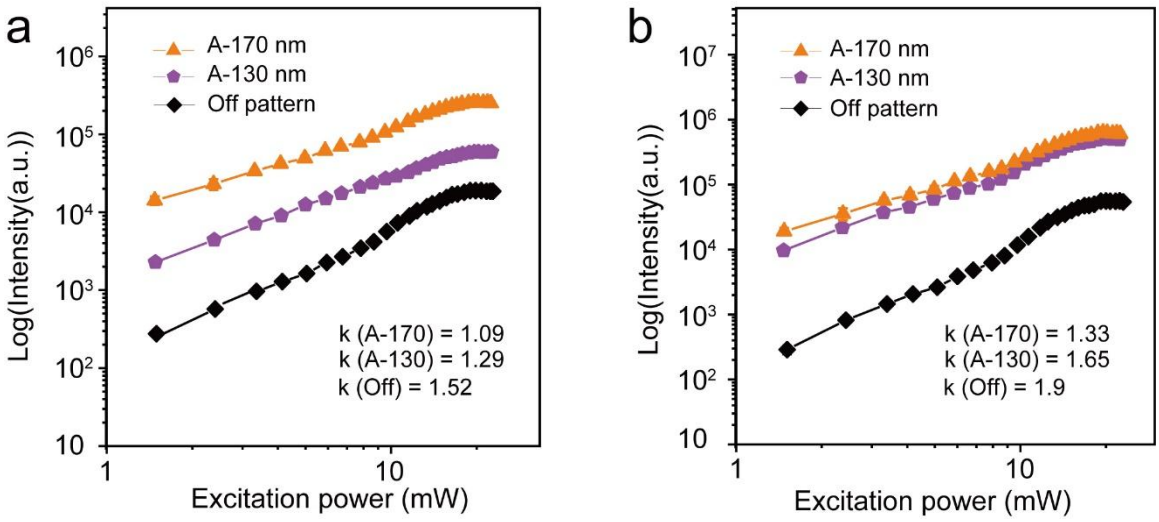

Figure S7. Power-dependent photoluminescence intensity measurements at 540 nm (**a**) and 655 nm (**b**) for three samples: UCNPs on Al film without antennas, UCNPs coupled with antenna-170, and UCNPs coupled with antenna-130.

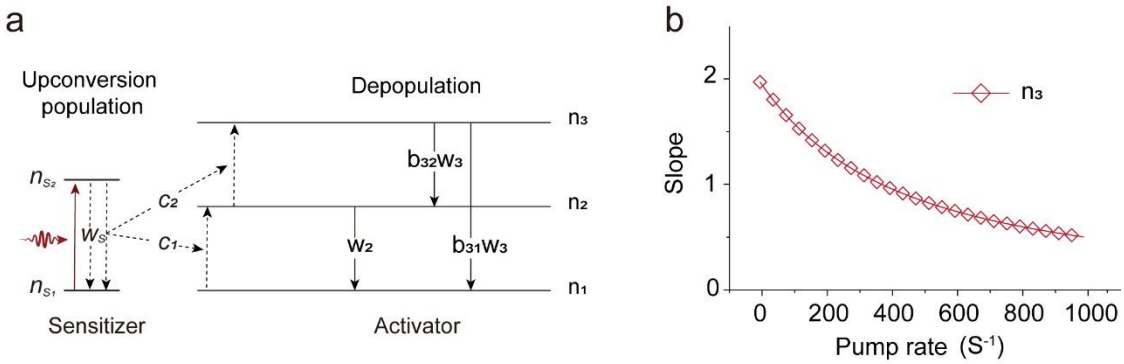

Figure S8. Numerical modelling of a general sensitizer-activator energy transfer upconversion system. (**a**) Simplified three-level energy diagram of an energy transfer upconversion system containing sensitizers and activators; W is the intrinsic decay constant, C_i denote the upconversion coefficients, and b_{ij} are the branching ratios. (**b**) Numerically simulated evolution of the sensitivity of upconversion luminescence intensity as a function of pump rate.

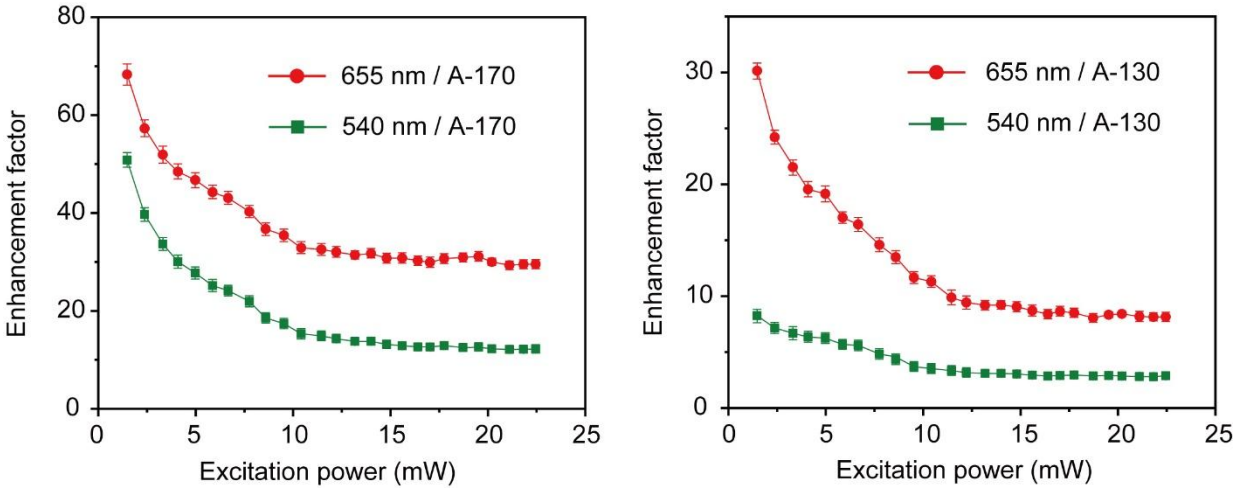

Figure S9. Power-dependent upconversion luminescence enhancement at 540 nm and 655 nm for UCNPs coupled with antenna-170 and antenna-130, respectively,

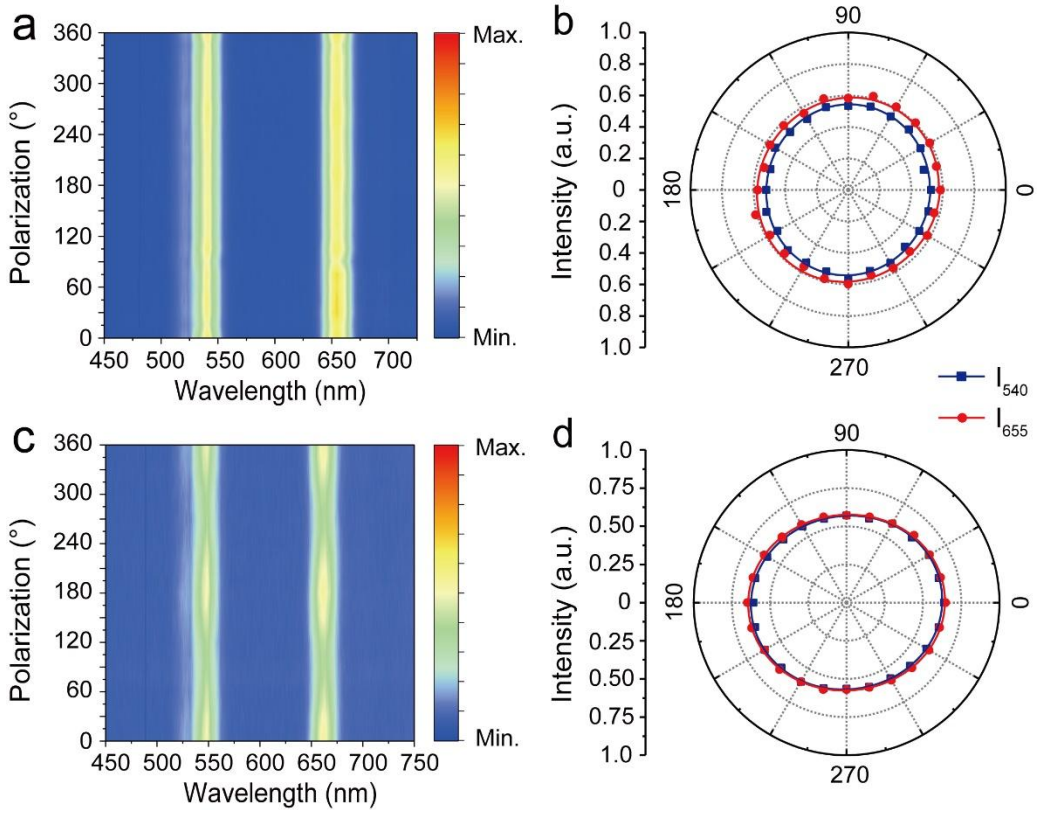

Figure S10. (**a,b**) Experimental upconversion emission spectra of UCNPs on an Al film without antennas as a function of excitation polarization angle and corresponding peak intensity polar plots. (**c,d**) Experimental upconversion emission spectra of UCNPs on an Al film as a function of the detection polarization angle and corresponding peak intensity polar plots.

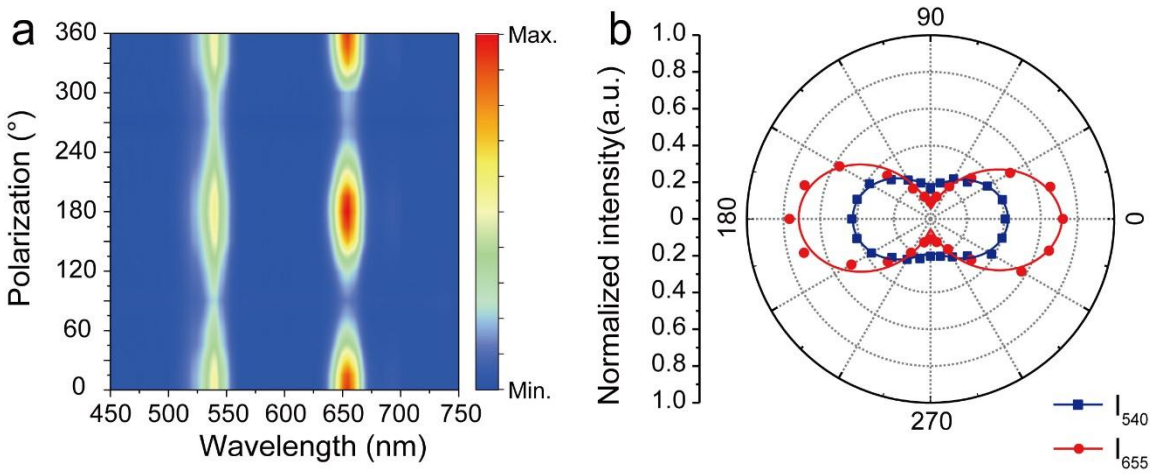

Figure S11. (**a**) Dependence of emission spectra of antenna-130-coupled UCNPs on the excitation polarization angle (θ). (**b**) Polar plots of upconversion peak intensity as a function of excitation polarization angle (θ).

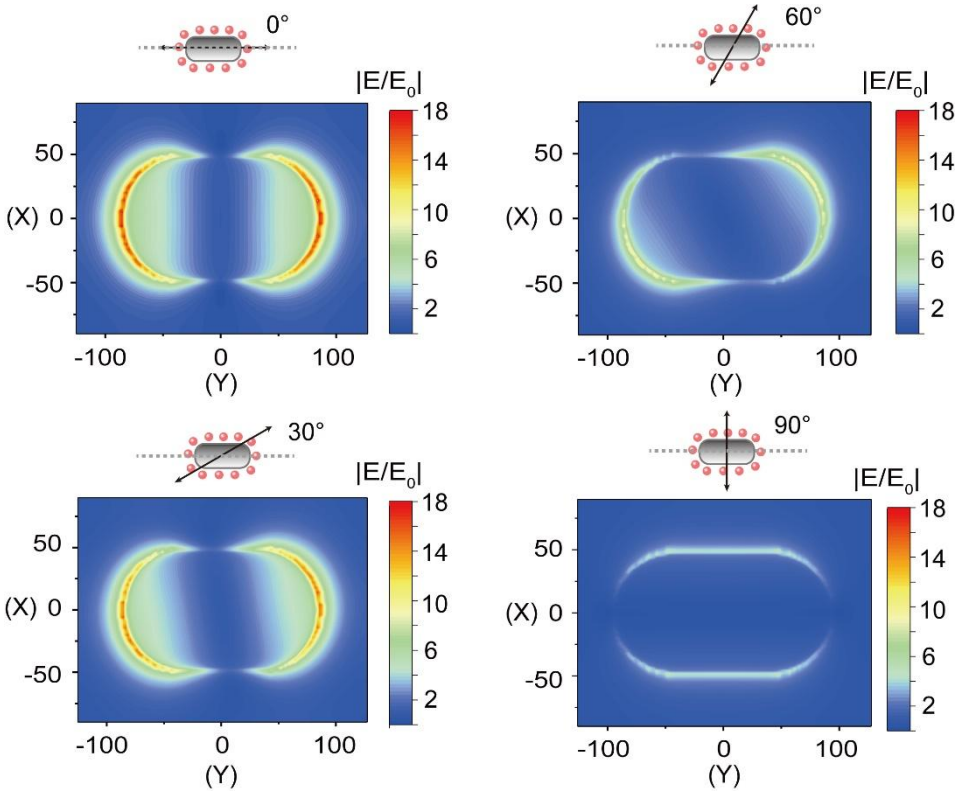

Figure S12. Simulated plasmonic near-field distributions of antenna-170 under different excitation orientations (the pump wavelength is 980 nm).

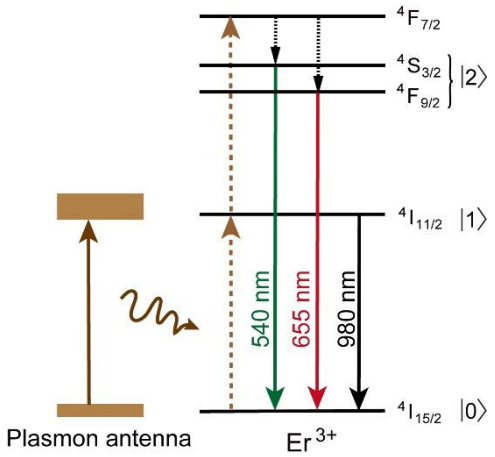

Figure S13. A simplified energy-level scheme for the ESA-mediated upconversion process, where |0>, |1> and |2> represent the ground level, intermediate level, and emission levels, respectively.

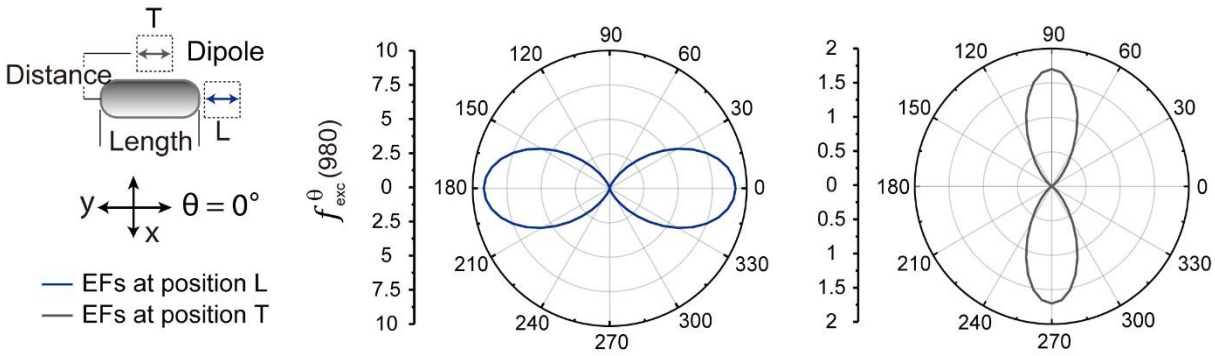

Figure S14. Simulation results for the polarization-dependent excitation enhancement factor (f_{ex}^{θ}) of dipole emitters arranged in longitudinal (L) and transverse (T) directions to rod antennas (antenna-130). The distance between the emitters and the antennas is set to 5 nm.

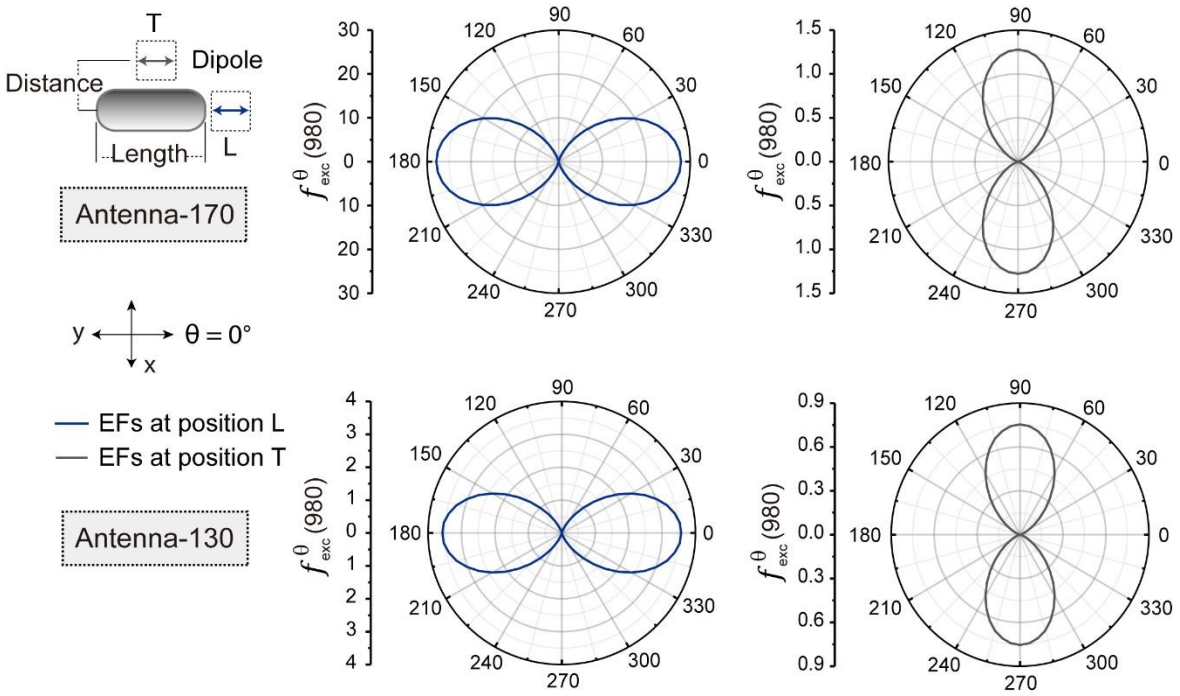

Figure S15. Simulation results for polarization-dependent excitation enhancement factor (f_{ex}^{θ}) of dipole emitters arranged in longitudinal (L) and transverse (T) directions to rod antennas. The distance between the emitters and the antennas is set to 10 nm.

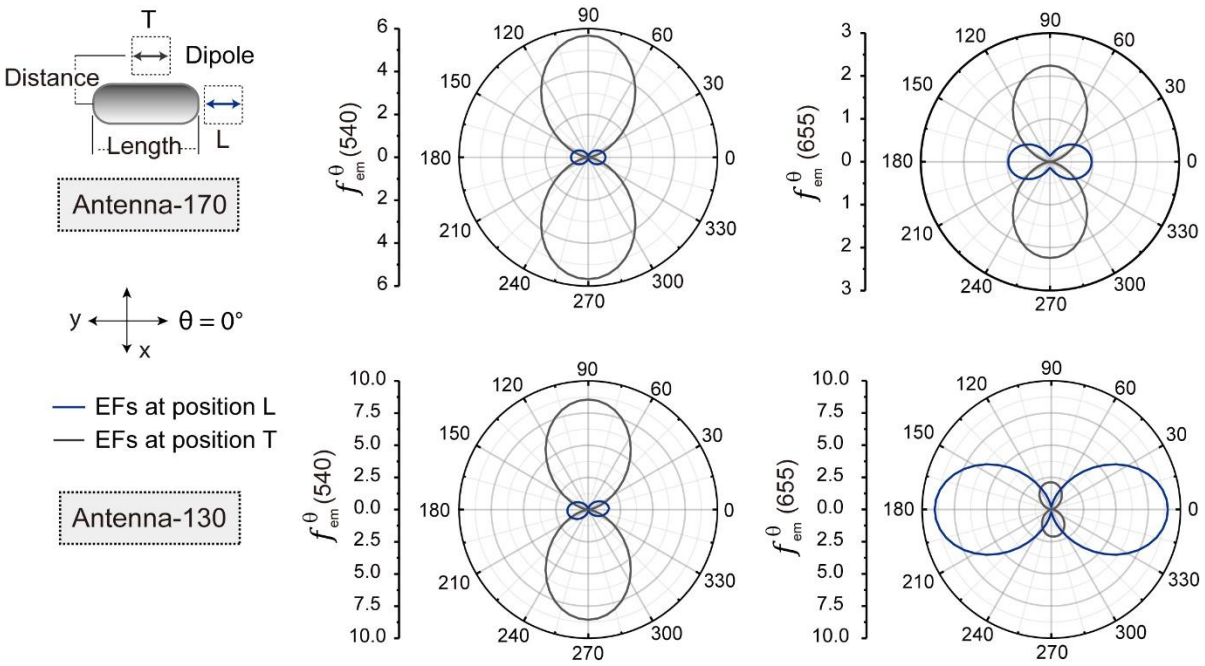

Figure S16. Simulation results for emission enhancement factors (f_{em}^{θ}) at two emission wavelengths of dipole emitters arranged in longitudinal (L) and transverse (T) directions to rod antennas. The distance between the emitters and the antennas is set to 10 nm.

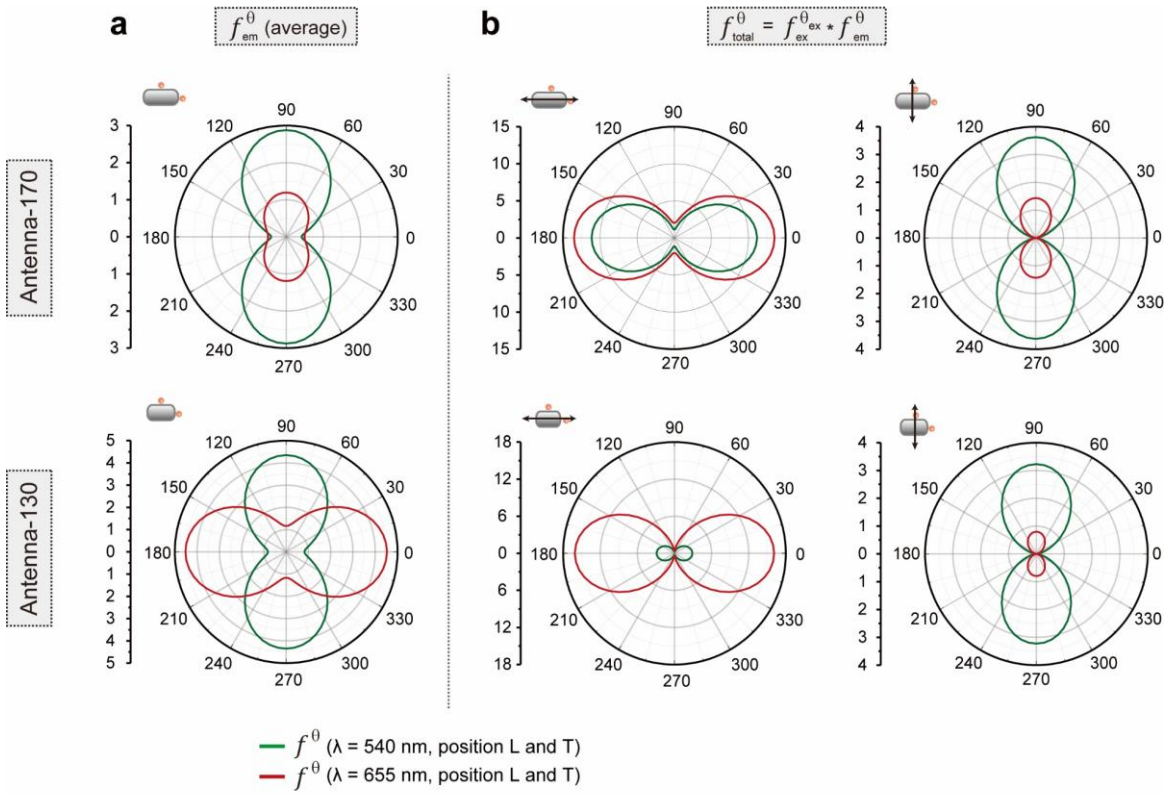

Figure S17. (**a**) Simulations of polarization-dependent average emission enhancement factors, f_{em}^{θ} (average), for dipole emitters with the emission wavelength at 540 nm and 655 nm. (**b**) Simulations of polarization-dependent total enhancement factors (f_{total}^{θ}) for dipole emitters with the emission wavelength at 540 nm and 655 nm. The separation distance between the emitters and antennas is set to 10 nm. The polar pattern of f_{em}^{θ} (average) was plotted by calculating the average value of f_{em}^{θ} at T and L locations, f_{em}^{θ} (average) $= \frac{f_{em}^{\theta}(L)+f_{em}^{\theta}(T)}{2}$, which showed a dominant polarization state along the transverse direction for the sample of antenna-170 and showed obvious anisotropic polarization properties in orthogonal directions for the sample of antenna-130. The total enhancement factors (f_{total}^{θ}) were calculated by integrating excitation and emission enhancements in both T and L positions, $f_{total}^{\theta} = \frac{f_{total}^{\theta}(L)+f_{total}^{\theta}(T)}{2}$. The symbol θ represents the orientation angle of the dipole source. θ_{ex} represents the excitation polarization angle.

Supplemental References

S1. Palik, E. D., eds. (1998). Handbook of optical constants of solids (Academic press), vol 3.

S2. Sokolov, V. I., et al. (2015). Determination of the refractive index of β-$NaYF_4$/Yb^{3+}/Er^{3+}/Tm^{3+} nanocrystals using spectroscopic refractometry. Optics and Spectroscopy *118*, 609-613. https://doi.org/10.1134/S0030400X15040190.

S3. Liu, X., and Lei, D.Y. (2015). Simultaneous excitation and emission enhancements in upconversion luminescence using plasmonic double-resonant gold nanorods. Scientific Reports *5*, 15235. https://doi.org/10.1038/srep15235.

S4. Xu, Y., Lee, R. K., and Yariv, A. (2000). Quantum analysis and the classical analysis of spontaneous emission in a microcavity. Physical Review A *61*, 033807. https://doi.org/10.1103/PhysRevA.61.033807.

S5. Gamelin, D.R., Gudel, H.U. (2001). Upconversion processes in transition metal and rare earth metal systems, H. Yersin, eds. (Springer, Berlin, Heidelberg), Transition metal and rare earth compounds. Topics in current chemistry, vol 214. https://doi.org/10.1007/3-540-44474-2_1.